Final results of the PERSEE experiment

J.M. Le Duigou[1], J. Lozi[1,2], F. Cassaing[2,7], K. Houairi[2,7], B. Sorrente[2,7], J. Montri[2,7], S. Jacquinod[3], J-M Reess[4,7], L. Pham[4,7], E. Lhome[4,7], T. Buey[4], F. Hénault[5], A. Marcotto[5], P. Girard[5], N. Mauclert[5], M. Barillot[6], V. Coudé du Foresto[4], M. Ollivier[3]

[1] : Centre National d'Etudes Spatiale
18 Avenue Edouard Belin
31401 TOULOUSE Cedex 9 – France
tel : (+33) 1 61 28 21 24
fax : (+33) 1 61 28 26 92
Jean-Michel.LeDuigou@cnes.fr
[2] : ONERA, the French Aerospace Lab
[3] : Institut d'Astrophysique Spatiale d'ORSAY
[4] : Observatoire de Paris
[5] : Observatoire de la Côte d'Azur
[6] : Thalès Alénia Space
[7] : Groupement d'Intérêt Scientifique PHASE (Partenariat Haute résolution Angulaire Sol Espace)

ABSTRACT: The PERSEE breadboard, developed by a consortium including CNES, IAS, LESIA, OCA, ONERA and TAS since 2005, is a nulling demonstrator that couples an infrared nulling interferometer with a formation flying simulator able to introduce realistic disturbances in the set-up. The general idea is to prove that an adequate optical design can considerably relax the constraints applying at the spacecrafts level of a future interferometric space mission like Darwin/TPF or one of its precursors. The breadboard is now fully operational and the measurements sequences are managed from a remote control room using automatic procedures. A set of excellent results were obtained in 2011. The measured polychromatic nulling depth with non polarized light is $8.8\ 10^{-6}$ stabilized at $9\ 10^{-8}$ in the 1.65-2.45 µm spectral band (37 % bandwidth) during 100 s. This result was extended to a 7h duration thanks to an automatic calibration process. The various contributors are identified and the nulling budget is now well mastered. We also proved that harmonic disturbances in the 1-100 Hz up to several ten's of nm rms can be very efficiently corrected by a Linear Quadratic Control (LQG) if a sufficient flux is available. These results are important contributions to the feasibility of a future space based nulling interferometer.

Keywords : Interferometry, Formation flying, Nulling, Exoplanets, Darwin, TPF, Pegase

1. INTRODUCTION

Although it has been recently postponed due to high cost and risks, nulling interferometry in space remains one of the very few direct detection methods able to characterize extrasolar planets and particularly telluric ones. Within this framework, several projects such as DARWIN [1], [2], TPF-I [3], [4], FKSI [5] or PEGASE [6], [7], have been proposed in the past years. Most of them are based on a free flying concept. It allows firstly to avoid atmosphere turbulence, and secondly to distribute instrumental function over many satellites flying in close formation. In this way, a very high angular resolution can be achieved with an acceptable launch mass. But the price to pay is to very precisely position and stabilize relatively the spacecrafts, in order to achieve a deep and stable extinction of the star. Understanding and mastering all these requirements are great challenges and key issues towards the feasibility of these missions. Thus, we decided to experimentally study this question and focus on some possible simplifications of the concept.

Since 2006, PERSEE (PEGASE Experiment for Research and Stabilization of Extreme Extinction) laboratory test bench is under development by a consortium composed of Centre National d'Etudes Spatiales (CNES), Institut d'Astrophysique Spatiale (IAS), Observatoire de Paris-Meudon (LESIA), Observatoire de la Côte d'Azur (OCA), Office

Optical and Infrared Interferometry III, edited by Françoise Delplancke, Jayadev K. Rajagopal, Fabien Malbet,
Proc. of SPIE Vol. 8445, 844525 · © 2012 SPIE · CCC code: 0277-786/12/$18 · doi: 10.1117/12.925350

National d'Etudes et de Recherches Aérospatiales (ONERA), and Thalès Alénia Space (TAS) [9],[10]. It is mainly funded by CNES R&D. PERSEE couples an infrared wide band nulling interferometer with local OPD and tip/tilt control loops and a system able to introduce realistic disturbances in the set-up. Although it was designed in the framework of the PEGASE free flying space mission, PERSEE can adapt very easily to other contexts like FKSI (in space, with a 10 m long boom structure) or ALADDIN [8] (on ground, in Antarctica) because the optical designs of all those instruments are very similar. After a short description of the experimental setup, we will present the experimental results of the cophasing systems and the measured polychromatic nulling ratio. A detailed analysis of the nulling budget is also presented based on various experiments performed on PERSEE.

2. DESCRIPTION OF PERSEE

This section provides the reader with a brief description of PERSEE. More details can be obtained by the interested reader from [9] - [13].

2.1. Goals

Starting from a state of the art nuller of the 2006-2007 period, PERSEE is an experimental attempt to better master the system flowdown of the nulling requirements both at payload (instrument main optical bench) and platform levels (satellites). The balance of the constraints between those two levels is a key issue. The more disturbances the payload can face, the simpler the platforms, the lower the cost. The general idea is hence to simplify as much as possible the global design and reduce the costs of a possible future space mission. The detailed objectives have been described in [9]. Our main requirement is to reach a 10^{-4} nulling ratio in the [1.65-2.4] µm band (about 40% spectral bandwidth) with a 10^{-5} stability over a 10 h time scale despite the injection of representative disturbances. Another important requirement is to be able to find and stabilize fringes, which have an initial drift speed (as seen from the interferometer core) up to 150 µm/s, as this can greatly simplify the relative metrology and control needs. We want to study and maximize the rejection of external disturbances introduced at relevant degrees of freedom of the optical setup by a disturbance module simulating various environments coming from the satellite level.

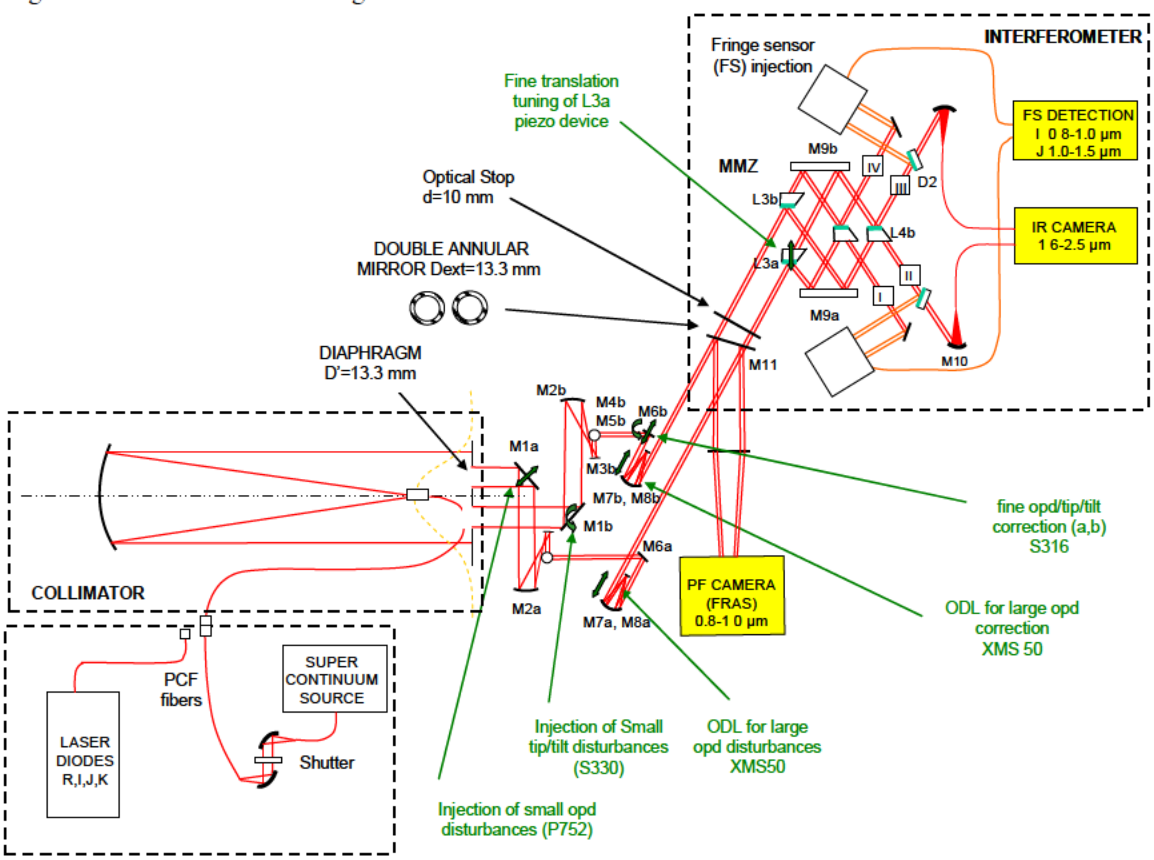

Fig. 1. General setup of PERSEE in the final operational state.

2.2. Optical setup

Fig. 1 gives an overview of the up-dated optical layout. Part of the real implementation of the PERSEE is illustrated by fig. 2. With respect to earlier versions, the source module was changed. It finally uses a super-continuum high power laser source covering a wide spectral range from 0.6 to 2.5 µm instead of three separate sources. The light is injected at the focus of a 100 mm diameter collimator (focal 750 mm) through a PCF fiber designed to be single mode in the full spectral range, but with a chromatic numerical aperture. The R subband ([0.6-0.8] µm) is used for alignment purposes. The I subband ([0.8-1] µm) is dedicated to the channel 1 of the Fringe Sensor (FS) and the Field Relative Angle Sensor (FRAS). The J subband ([1-1.5] µm) is dedicated to the channel 2 of the FS. The nulling rate is measured in the H+K band ([1.65-2.5] µm). The two 40 mm beams (a and b) coming out of the separation module first encounter two 45° fold mirrors (M1) simulating the siderostats of PEGASE [6]. Accurate calibrated disturbances can be introduced at this level either in tip/tilt (few tens of mas resolution) or OPD (nm resolution). In the full design presented below, the optical train incorporates afocal systems with M = 3 magnification to reduce the beam size down to about 13 mm, which is a feasible size for the combining part. These devices were necessary first to simulate the possible effects of this optical function (M=20 to 40 in PEGASE) then to get enough photons with the original source design, which used a much weaker source in the K band. As the source was changed to a more powerful one, the second reason to implement the afocal compressors is no more valid. All presented results were made without the afocals, directly taking a 13 mm pupil from the collimator to the M1 mirror. The study of their possible effect on the performance is postponed to a later step as this is supposed to be a second order contributor.

The M4 mirrors deviate the beam toward the -Z direction. Coupled with the M1 mirrors, they create a “field reversal” achromatic phase shift (APS) between the two arms. This is the most efficient way to implement this optical function as it doesn’t require additional dispersive optical parts. Following, each arm has a cat’s eye optical delay line (ODL, 50 mm stroke and 10 nm resolution) and a 30° active M6 mirror acting both in tip/tilt and fine OPD (12 µm or 240 arcsec stroke, 0.2 nm resolution). These active systems can all together generate various corrections covering the necessary range and resolution both in tip/tilt and OPD. They are used in dedicated control loops, which use the FRAS camera for the tip/tilt and the FS for the OPD. The optical stop is placed after the ODL. The design of the ODL (second mirror curvature) is made to optically conjugate the stop and the M6 mirrors. In this way, the coupling between the opd and tip/tilt degrees of freedom is minimized. Due to the excellent quality of the MMZ manufacturing, a chromatism compensator before the combining stage was finally not necessary.

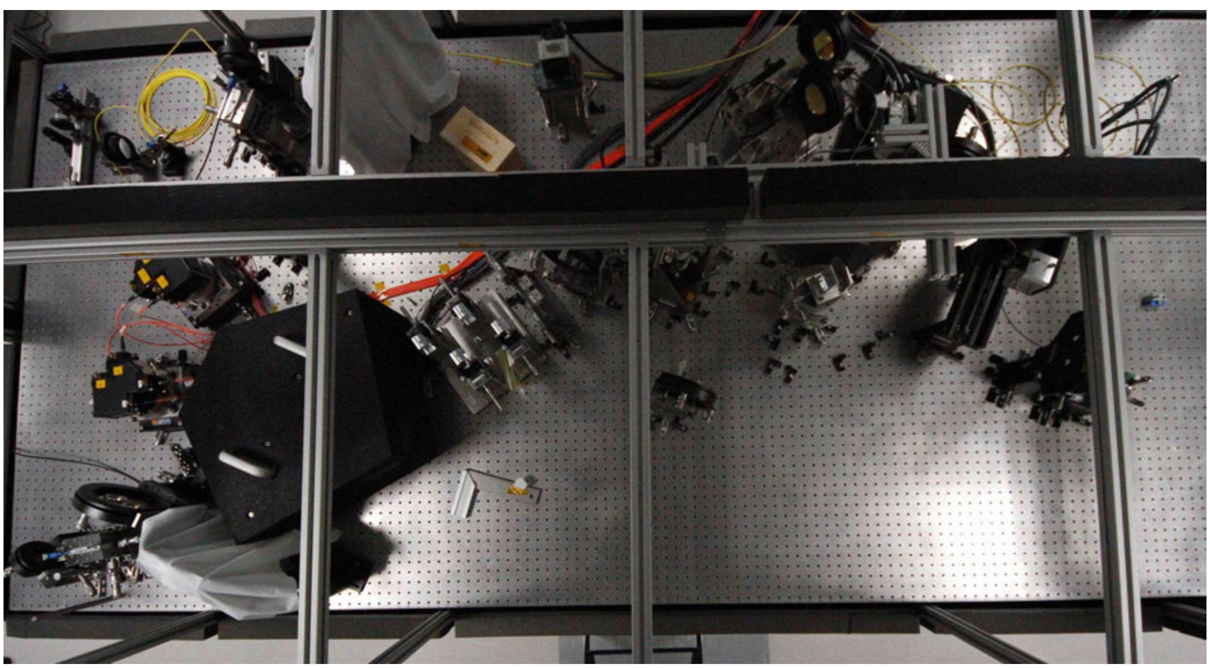

Fig. 2. Top view of the real implementation, optical train and MMZ (the source module source and the camera are implemented on separate optical tables)

The combination stage is a kind of Modified Mach-Zehnder (MMZ) [14] with two inputs (a and b arms) and four outputs (I to IV). Due to some symmetry and optical tight tolerances (geometry and coatings), the setup guarantees that two outputs are achromatic. The four beam splitters have a trapezoidal geometry [12] to avoid stray light. They have a specifically designed three-layer coating of about 200 nm thickness, which allows to achieve appropriate reflection and transmission coefficients for both polarizations in the whole K+H band. The beam splitters are divided into two groups as compared to the classical setup [14]. This allow to translate the L3a component without impacting the nulling output (output III). The translation is adjusted so that the four outputs generate four points in the I and J fringes roughly with a $\lambda/4$ spacing, which allows a spatial ABCD-type fringe tracking algorithm. The tip/tilt degrees of freedom of L3a are used to maximize the contrast in the FS A and C outputs (I and IV). This compact design allows to minimize differential optical path between FS and nulled output down to about 10 cm. This point is critical because it relaxes the stabilization requirements at system level.

After the MMZ, dichroic plates separate the various spectral channels and direct them into appropriate detection chains via injection into optical fibers. The FS detection is made of a set of eight monopixels and multimode fibers. The chromatism of the injection lenses makes the FS spectral bands sensitive to the alignment of these lenses. For the K channel, the light is injected in a fluoride glass single mode fiber. The detector is a nitrogen cooled infrared camera based on a Teledyne picnic matrix behind a dispersive element, which allows to have polychromatic measurements of both dark and bright fringes at the same time. A calibrated optical attenuator is used in the bright output to optimize the dynamic of both outputs with respect to the detector well depth.

3. EXPERIMENTAL RESULTS OF THE COPHASING SYSTEM

3.1 Tip/tilt under laboratory environment

The tip/tilt of each arm for the science channel is optimized to maximize the coupling into the single mode fiber of the nulled output (III). At the beginning of each measurement sequence, a calibration procedure [16] is performed to find the reference position for each arm. Then a control loop maintain the position around this reference. This loop is based on the M6 mirrors, the FRAS camera and a classical integrator as the control law. The camera measures the flux of an annular section of the beams in the I band. The maximum reading frequency of the camera is 200 Hz.

The open loop noise is about 500 mas and is dominated by the turbulence effect at low frequency as shown on fig. 3. The tip/tilt is not very sensitive to the laboratory disturbances and is easier to control than the opd. Furthermore, we did not try to inject calibrated disturbances in tip/tilt because this is far less critical than on the opd.

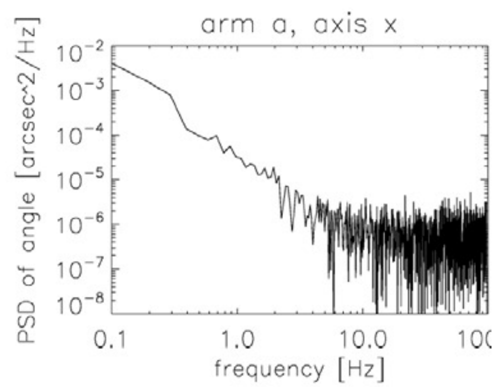

Fig. 3 : Tip/tilt noise (open loop)

As the contributors beyond 5 Hz are very low, the gain of the closed loop can be set to a low value (0.05). The maximum cutting frequency is about 10 Hz. Using the maximum flux of the source, the closed loop performance obtained is 56 mas rms, about 1/100th of the pixel size (6 arcsec). Fig 4 shows the decrease of this performance with the photon count. As expected, we find a $N^{-1/2}$ slope, which shows that our set-up is photon-noise limited as expected. The initial requirement of 600 mas can be reached for 2 10^5 ADU (total for the image of the point source in one arm, including the optical transmission and the quantum efficiency of the detector).

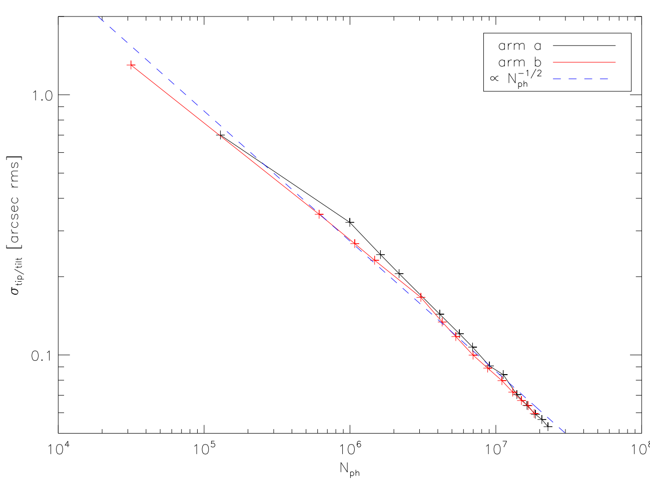

Fig. 4 : Tip/tilt noise as function of flux (closed loop)

3.2 Opd under laboratory environment

The opd is much more sensitive to mechanical disturbances coming either from the laboratory or from a calibrated disturbance. During the step by step integration progress, the various vibrations coming from the environment were characterized. In the most favorable case, without transient event (no aircraft flying above the campus, no subway passing underground, nobody closing a door or walking in the nearby rooms,…), we measured the PSD of the opd noise of fig. 5a (black curve), with an overall level of 1.1 nm rms. At low frequency, the PSD is dominated by the turbulence.

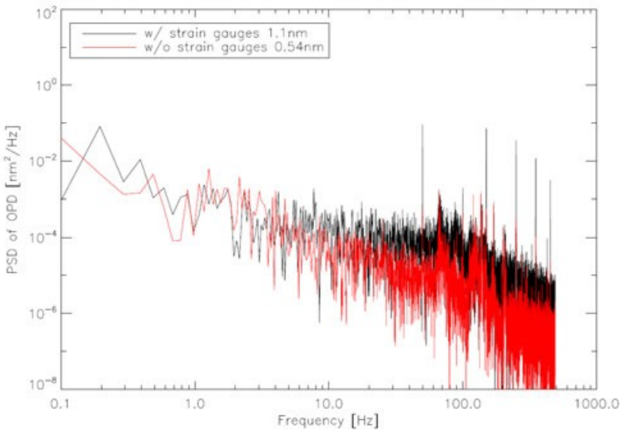

Fig. 5a : opd residual noise, open loop

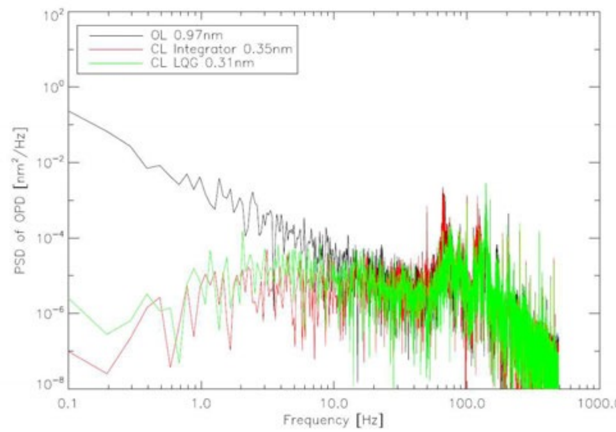

Fig. 5b : closed loop compared to open loop, integrator or LGQ

The power supply is responsible for the 50 Hz very narrow peak and the associated harmonics. The other broader peaks are due to vibration modes of the optical mounts : ODL (80 Hz), MMZ (130 to 170 Hz), M6 (110 Hz), are excited by low frequency disturbances from the building. The M6 piezo-electric devices have strain-gauges to control their position. They are responsible for an additional noise as can be seen on the black curve as compared to the red one on fig. 5a. The air-conditioning and over-pressure systems were OFF during this measurement. As the associated machinery is located at the same level of the building, it generates quite high vibrations (5- 6 nm rms each). They are not compatible with our goals and we had to shut them down during all measurements. The drawback is that we had to perform regular calibrations of the experiment because the temperature slowly drifts.

Two control laws were implemented: a simple integrator or a more complex Linear Quadratic Gaussian (LQG) controller. Details of the LQG implemented in PERSEE can be found in [15]. It uses an a priori model of the disturbances structure: a low frequency part corresponding either to the turbulence (ground) or to a residue of the GNC control (space mission), a number of harmonic functions represented by second order systems, and a high frequency measurement noise. Using the open loop measurement, an identification is performed using this a priori model to estimate the various parameters (frequency, damping and level of harmonic functions, level of the noise, low frequency level). This information is then used within a Kalman filtering to optimize the control loop. The performance of this type of control is highly related to the quality of the disturbance model used.

When applied to the “natural” environment of the laboratory, both controllers have similar results as the disturbance to correct is very low. The residual opd noise is reduced down to 0.3-0.35 nm rms. Associated with the very good tip/tilt performance, the PERSEE set-up provides excellent conditions for accurate nulling measurements.

3.3 Opd under calibrated disturbances.

One very important feature of PERSEE is the ability to inject calibrated disturbances simulating a real in-flight environment. Up to now only the small displacements part is implemented and tested. As the principles are the same for both tip/tilt and opd, the experimentation was limited to opd because it is far a more sensitive parameter for the nulling ratio. But the results could easily be translated to the two other degrees of freedom if they were supposed to face important disturbances in flight.

From the PEGASE phase 0, we derived various disturbances cases. The GNC is supposed to perform a first control of the satellites relative and absolute positions. The foreseen architecture involves a continuous control on the siderostats with 3 reaction wheels as actuators and a pulsed control on the combiner with an actuation period of about 100 s. The

GNC damps the relative movement of the satellites and reduces the opd noise in the control band (1 Hz) to an acceptable level for the optical payload ([17]). The first contributor to consider is then a low frequency term below 1 Hz. In the worst case it was estimated to 3 nm rms.

Following, as the reaction wheels are rotating machines with imperfect balance, they generate an harmonic disturbance composed of a fundamental sine function at the wheel speed and various harmonics linked to the geometry of the bearings. In some cases, a coincidence may occur between one of the harmonics of one of the 6 wheels and a structural mode. No detailed model was built, but the following hypothesis were made on base of CNES previous experience in the field of microvibrations ([18]): wheel speed 1, 3.5 or 4.5 Hz, first solar array mode at 15 Hz (they lay on quite rigid sun-shades, [7]), first siderostat global mode at 55 Hz (300 Kg quite compact satellite), first local mode of M1 mirror assembly at 75 Hz, first local mode of the wheels supporting structure at 85 Hz. To obtain worst cases, multiple coincidence are allowed. The most conservative case is illustrated by fig. 6. The black curve is the injected disturbance without correction. The overall level is 18 nm rms. Both control laws can face the low frequency part efficiently. But only the LQG can significantly reduce the effect of the amplified wheels harmonics and reduce the overall level down to 0.77 nm rms.

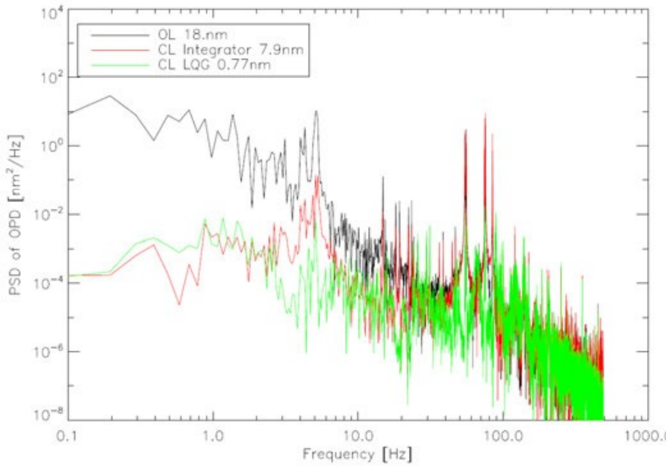

Fig. 6 : opd noise as function of flux (closed loop with integrator or LQG compared to open loop)

Systematic tests were performed to test the robustness of the process with respect to the amplitude of each sine function, the frequency separation and the number of harmonics. The LQG performs very well even with a single harmonic up to 100 nm, two harmonics as close as 0.1 Hz and 20 harmonics of 10 nm each. These results are only possible if a high flux is available as this allow a high bandpass (1 KHz sampling frequency). This is the case with the super-continuum source on the experimental set-up. When reducing the flux, the measurement noise increases as illustrated by fig. 7. N_{ph} is the total number of photons detected in the SF I channel (2 arms, 4 outputs, quantum efficiency included). At very low flux, the noise is dominated by the detectors noise, as expected. In the high flux domain, the experimental law is N_{ph}^{-1} instead of the $N_{ph}^{-1/2}$ expected one. This might come from the statistics of the source optical power noise, which variance was measured to be proportional to the square of the average power (non linear effects in the PCF fiber) or from the noise of the electronic amplifiers used in the FS. In the test set-up, the required performance can be reached for 3 10^5 photons in the I band (SNR of 440).

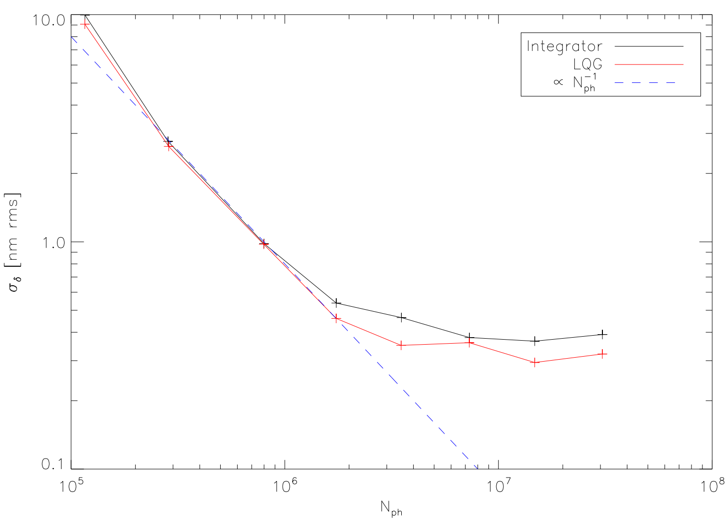

Fig. 7 : opd noise as function of flux (closed loop)

4. EXPERIMENTAL NULLING RESULTS

4.1 Mathematical background.

The extinction ratio is defined as:

$$N(\lambda,t)=I_{min}(\lambda,t)/I_{max}(\lambda,t). \quad \text{(Eq. 1)}$$

This quantity can be averaged over a spectral band ($<N>_\lambda$) or over a time duration ($<N>_t$), or both. σ is used for the associated variance. I_{min} and I_{max} are the minimum and maximum intensity of a fringe pattern as a function of opd. The total spectral range is divided into 9 bands (i=1..9). A detailed mathematical formulation is derived in [19] and was used as a basis of our nulling budget, but with some extension to take into account the spectral analysis. An important point is that the opd can not be optimized to minimize the extinction ratio of all spectral bands simultaneously. The ideal position is opd=0, but due to imperfect calibration between the FS and the nulled output, the FS reference position has to be set to a value δ_{ref}, which is not zero but experimentally minimize the average extinction rate on the whole band. This reference position is sensitive to temperature changes and has to be calibrated regularly. This is related to the thermo-elastic unstability of the uncommon optical paths in the MMZ. Let δ_i be the opd offset wrt to δ_{ref}, which minimizes the extinction ratio for the specral band i and λ_i its central wavelength. δ_i and λ_i are measured during the calibration process [16]. The intensity of arm a (b) coupled into the single mode fiber writes :

$$I_{a\text{ or }b,i} = I_{a\text{ or }b,i,max} \, [\, 1- 1/5\, (\pi D\theta_{a\text{ or }b}(t)/\lambda_i)^2]. \quad \text{(Eq. 2)}$$

$I_{a\text{ or }b,i,max}$ is the maximal intensity coupled into the fiber obtained for the tip/tilt reference position $(\alpha , \beta)_{a\text{ or }b,ref}$ during the tip/tilt calibration process. $\theta_{a\text{ or }b}(t)$ is the difference between the tip/tilt current position and this reference position (norm of (α , β)) . It is the residual noise of the tip/tilt control loop. D=10 mm is the diameter of the collimated beam before injection into the fiber.

The main contributors of the time averaged extinction ratio in the spectral band i are :

- opd
  - * chromatism main term : $(\pi\delta_i/\lambda_i)^2$
  - * opd noise : $(\pi\sigma_\delta/\lambda_i)^2$ where σ_δ is the opd noise as measured on the SF
  - * coupling term : $(\pi/\lambda_i)^2(\delta_{ref}^2 +2\ \delta_i\, \delta_{ref})$
- intensity mismatch
  - * quasi-static term : $\varepsilon_{i,stat}^2/4$, where $\varepsilon_{i,stat}=(I_{b,i}-I_{a,i}) /(I_{b,i}+I_{a,i})$
  - * noise : $1/400\ (\pi D/\lambda_i)^2\ [\theta_b (t)^2- (\theta_a (t)^2]$
- Polarization
  - * rotation : $\alpha_{i,rot}^2/4$, where α_{rot} is the differential rotation angle of the polarization between arm a and b as measured in band i.
  - * s-p delay : $\alpha_{i,s-p}^2/4$, where α_{s-p} is the differential delay between s and p polarization state

4.2 Monochromatic light.

The results in the monochromatic case are presented in [20]. They were performed on an intermediate configuration limited to the MMZ used in an auto-collimation set-up with laser diodes injected from the outputs of the set-up and reflected back by the M6 positioned at the entrance of the MMZ. The best obtained nulling ratio over a 100 s duration is 5.6 10^{-6} (temporal average over 100 s). The opd contribution accounts only for 3.10^{-7}. Many effects due to the imperfect calibration limited the performances. Each of them was addressed before proceeding to the polychromatic measurement.
In the monochromatic configuration, the sensitivity of the MMZ to temperature variations could be measured. The dephasing between output III and IV is a good indicator of the differential path between the nulling output in H+K band and the FS channels in the I and J bands. It proved to be perfectly correlated to the temperature variations as measured on the MMZ. The measured coefficient is 1200 nm/°C. The value for the final configuration is twice less, 600 nm/°C (one way only). This high sensitivity comes directly from the standard mounts used for the MMZ and also from the stability of the mechanism under the L3B beam splitter. A much more stable structure with much less adjustable degrees of freedom was planned, but was too costly for the project. Our estimation is that with an appropriate design, the thermal sensitivity of the differential opd could be reduced by at least a factor of ten.

4.3 Some calibrations aspects

Spectral calibration

The quantities λ_i and $\Delta\lambda_i$ for each spectral channel were measured using a Fourier transform analysis. They depend on the SF injection lens chromatic properties and a calibration is required. $\Delta\lambda_i/\lambda_i$ ranges from 7 to 11 %. The total spectral width is defined as :

$$\frac{\Delta\lambda_{moy}}{\lambda_{moy}} = \frac{(\lambda_9 + \Delta\lambda_9/2) - (\lambda_1 - \Delta\lambda_1/2)}{\lambda_{moy}} \qquad \text{(Eq. 3)}$$

$$\frac{\Delta\lambda_{moy}}{\lambda_{moy}} = 37\ \%\ \text{with}\ \lambda_{moy} = 2.0\ \mu\text{m}.$$

I_{max} measurement

I_{min} is measured on the output III when the opd is 0. The flux is dispersed on a 9 x 2 pixels zone of the PICNIC detector. I_{max} is the intensity we would have on the central fringe without the π phase shift. As the optical source has power variations of about 10 %, I_{max} has to be measured at the same time as I_{min} to have accurate results. Furthermore, as I_{max} is at least 10^4 greater than I_{min}, we used an optical attenuator in the bright output to match the dynamic of the IR camera.

In the original design, I_{max} was supposed to be measured on the output II of the MMZ using an optical attenuator (second 9 x 2 pixel zone on the camera). But due to the absorption coefficient of the coatings in the MMZ, the output II is not a fully constructive fringe when output III is a destructive one. There is a phase shift of about -20°. Hence I_{max} is sensitive to opd variations and is not constant in time. Furthermore, getting an excellent coupling ratio in both single mode fibers generates very stringent alignment constraints on the optical set-up. That's why, we decided to use another reference. An unused portion of the output pupil of the collimator is measured at the same time as I_{min} measurement. This I_{ref} is proportional to I_{max}. The coefficient is measured through the calibration process.

4.4 Polychromatic light.

Results over 100 s under the laboratory environment

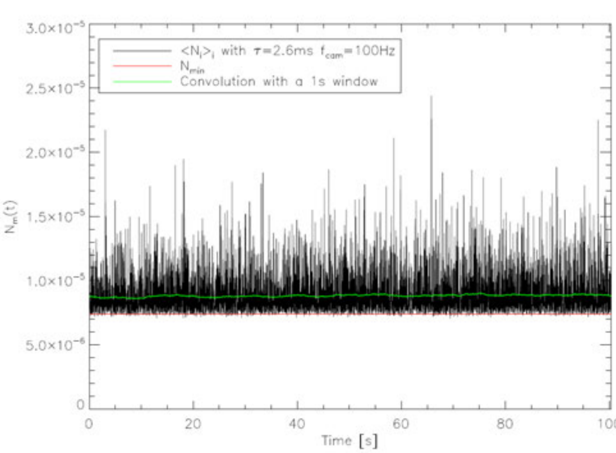

Fig. 8a : spectrally averaged null as a function of time

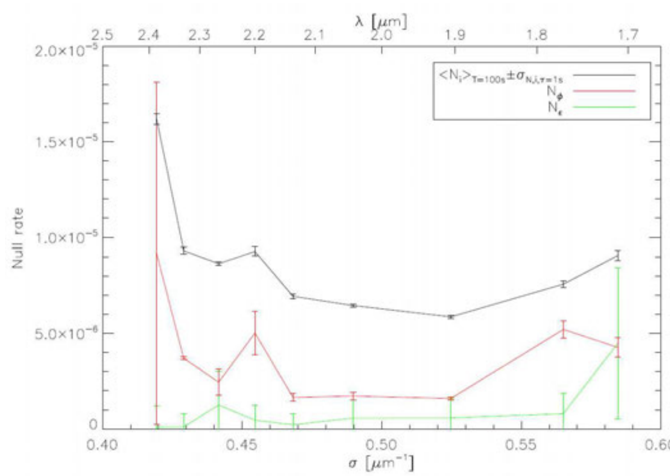

Fig. 8b : time averaged extinction ratio in each spectral channel

The best measurements obtained under the laboratory "natural" environment with the LQG based control on the opd and the integrator control law on the tip/tilt are illustrated by fig. 8a and 8b. The left graph is the temporal evolution over 100 s of the spectrally averaged extinction ratio. The black curve is the raw measurement with a reading frequency of the camera of 100 Hz and a τ=2.58 ms integration time. The green is the convolution with a 1 s window. We finally measure:

$$<<N>_{i=1..9}>_{T=100s} = \mathbf{8.8\ 10^{-6}} \text{ with the associated variance } \sigma_{t=2.58\,ms} = \mathbf{1.5\ 10^{-6}}$$

Reducing the frequency band by a convolution with a 1 s window reduces the variance to $\sigma_{\tau=1\,s}=\mathbf{9\ 10^{-8}}$
On the right hand, the black curve is the temporal average of the extinction ratio as a function of wavelength (or wave number). It shows that the set-up has very low chromatism effects. The last spectral channel has a degradation of the nulling extinction mainly due to a poorer SNR. It comes from the upper limit of the source spectrum, which is 2.4 µm. The red curves is the sum of the opd effects. Each one was estimated separately, using the FS data for the opd noise (0.74 nm rms noise), the chromatism measured during the calibration, the estimation of δ_{ref} by a statistical analysis of the data. The green one is the sum of the intensity mismatch effects, which were estimated from the FRAS measurement (65 mas rms noise)

$\langle N_{moy}\rangle_{T=100s}$	10^{-4}	$8,8\times10^{-6}$
$\langle N_{\phi}\rangle_{T=100s}$	7×10^{-5}	$3,9\times10^{-6}$
$\langle N_{\delta,w}\rangle_{T=100s}$	$3,5\times10^{-5}$ (both rows)	$1,4\times10^{-6}$
$\langle N_{\delta,ref}\rangle_{T=100s}$		10^{-7}
N_{σ}	$3,5\times10^{-5}$	$2,4\times10^{-6}$
$\langle N_{\varepsilon}\rangle_{T=100s}$	2×10^{-5}	$9,5\times10^{-7}$
$N_{\varepsilon,stat}$	2×10^{-5} (both rows)	$9,5\times10^{-7}$
$\langle N_{\varepsilon,dyn}\rangle_{T=100s}$		$7,9\times10^{-12}$
$N_{pol}{}^{a}$	10^{-5}	$3,9\times10^{-6}$
$\sigma_{N,\tau=1s}$	$1,5\times10^{-5}$	9×10^{-8}
$\sigma_{N,\delta,\tau=1s}$	$1,5\times10^{-5}$	10^{-7}
$\sigma_{N,\varepsilon,\tau=1s}$	3×10^{-6}	9×10^{-13}

$\langle N_{moy}\rangle_{T=7h}$	10^{-4}	$1,02\times10^{-5}$
$\langle N_{\phi}\rangle_{T=7h}$	7×10^{-5}	$4,6\times10^{-6}$
$\langle N_{\delta,w}\rangle_{T=7h}$	$3,5\times10^{-5}$ (both rows)	$1,4\times10^{-6}$
$\langle N_{\delta,ref}\rangle_{T=100s}$		$9,1\times10^{-7}$
N_{σ}	$3,5\times10^{-5}$	$2,3\times10^{-6}$
$\langle N_{\varepsilon}\rangle_{T=100s}$	2×10^{-5}	$5,5\times10^{-7}$
$N_{\varepsilon,stat}$	2×10^{-5} (both rows)	$5,5\times10^{-7}$
$\langle N_{\varepsilon,dyn}\rangle_{T=100s}$		$7,9\times10^{-12}$
$N_{pol}{}^{a}$	10^{-5}	$5,0\times10^{-6}$
$\sigma_{N,\tau=1s}$	$1,5\times10^{-5}$	6×10^{-7}
$\sigma_{N,\delta,\tau=1s}$	$1,5\times10^{-5}$	6×10^{-7}
$\sigma_{N,\varepsilon,\tau=1s}$	3×10^{-6}	9×10^{-13}

Table 1a and b : theoretical (column 1) and experimental (column 2) nulling budget, spectrally averaged, temporally averaged over 100 s (left) or 7 h (right)

The spectral averaging of this data and a very detailed analysis of the various contributors lead to table 1a, which compares the experimental average nulling budget with the allocations.

The intensity mismatch has low impact on the extinction ratio in our set-up because of the high performance of the tip/tilt system. The static part proved to be constant over the spectral band and amounts 0.2 %, which is far less than the requirements of 1 %. This could be achieved by a fine calibration using the orientation of the PCF at the focus of the collimator. The low tip/tilt noise of 65 mas rms results in a very low contribution to the nulling variance. The intensity mismatch has a very low noise well below 0.1 % rms.

Thanks to the LQG algorithm, the opd noise is below 1 nm rms (0.74 nm rms). Its contribution to the average nulling ratio is limited to 1.4 10^{-6}. The dominant term is the chromatism effect, which reaches 2.4 10^{-6}. It is mainly due to the imperfect realization of the MMZ beam splitters. Fig. 9 shows a simulation of a polychromatic nulling ratio with a 0.2 µm thickness difference between L3a and L4b, superposed with a non uniformity error of the 3 layers coating of variable amplitude (eps is per layer). We know from dedicated measurements that the maximum thickness error is below 0.28 µm considering a set of 9 manufactured beam splitters. This is a pessimistic figure but we don't know the error for the real L3b/L4b pair implemented on the bench. The comparison with the measured data is difficult because the various defaults may combine differently, but a value of eps below 0.25 nm, as specified, is coherent with the low chromatism observed.

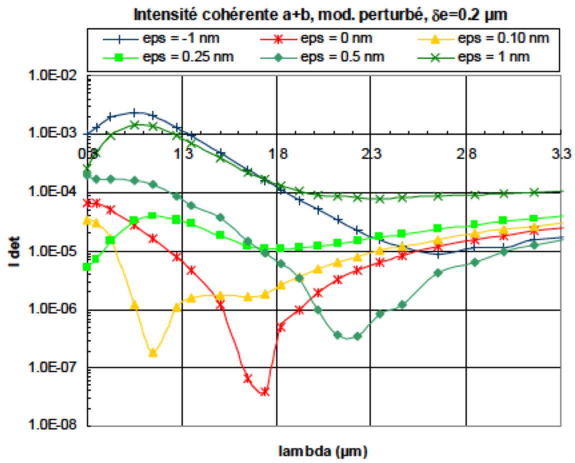

Fig. 9 : simulation of the impact of beam splitters defaults on the nulling ratio

between 1.5 and 2.5 µm. Both the coating uniformity and the beam splitters thickness have been mastered to un excellent level by the manufacturer.

The polarization effects are only estimated by the complement of the other effects. They are roughly of the same level as the opd contribution. We can not separate the rotation effect from the s-p effect. Assuming the rotation effect alone, the obtained static contribution corresponds to a 14 arcmin rotation between arm a and b for one polarization direction. With the s-p effect only, it corresponds to 2.5 nm opd difference of s wrt to p. A dedicated test was performed to estimate the effect of differential angles in the two arms. A variable tilt angle was applied on M1a and the associated correction made on M6a, while the mirrors of the other arms were set to their neutral position. For each value, the opd was automatically adjusted to minimize the nulling ratio. Fig. 10a and b compare the simulation with the measurement.

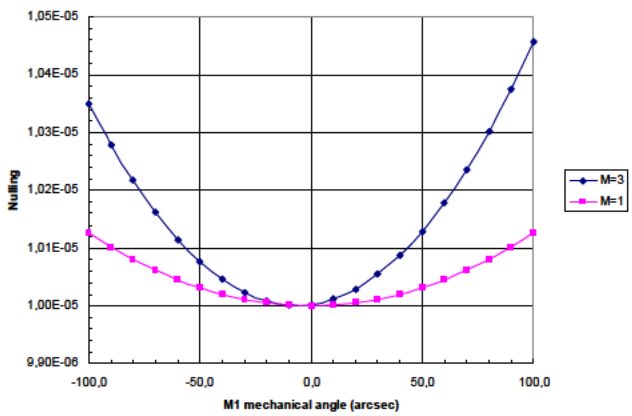

Fig. 10a : monochromatic nulling ratio as a function of M1 tilt, simulation of the test set-up, 10^{-5} mean nulling superposed

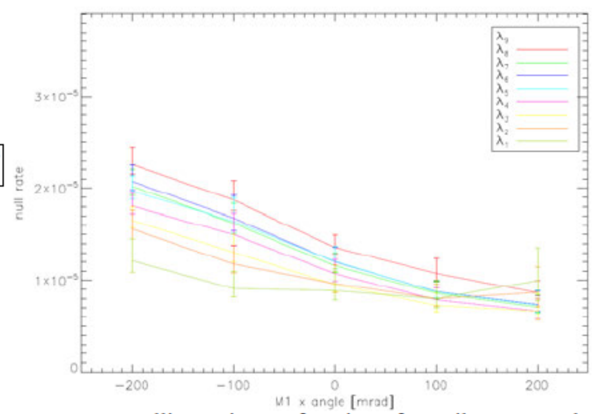

Fig 10b : nulling ratio as a function of M1 tilt, 9 spectral bands

As the law is of quadratic type, a coefficient can be fitted. The theoretical value is 1.25 10^{-11} $arcsec^{-2}$ while the experimental one is 4 time greater. This probably comes from the fact that when M1 is tilted, the portion of the associated beam at the output of the collimator moves in a Gaussian shape. The flux mismatch is no longer optimal when M1 moves. Furthermore, this Gaussian shape is not constant with the wavelength because the ON of the PCF is chromatic. That's why a important chromatic effect can be seen on fig. 10b. A more complicated measurements procedures is planned to disentangle the various effects, but it is not yet implemented. We can nevertheless already conclude that tip/tilt values of up to 200 arcsec of relative depointing between pairs of mirrors are acceptable for a 210^{-5} nulling rate.

Results over a 7 h period under laboratory environment

The measurements were extended to a 7 h duration during a night test and results are presented in table 1b. During the test the ambient temperature of the laboratory decreased regularly with a mean slope of – 13 µK/s (from 21.13 to 20.61 °C). As the MMZ and the optics are under a thermal protection, this slope is slightly lower at the MMZ level: -11 µK/s, which translates to – 7 pm/s on the differential opd between the SF and the science channel using the coefficient measured previously (see 4.2). The SF calibration is automatically performed every hour resulting in a new interaction matrix between the 8 outputs and the estimated parameters (arms flux in I and J bands, opd). The tip/tilt and opd reference points are automatically updated every 100s using a dithering method. This calibration lasts about 30 s. Almost all contributors to the nulling budget obtained this way are very close to their value over a 100s period, except one: the bias effect in the reference position of the FS, which is ten times higher and becomes a important contributor. This is because δ_{ref} has a mean drift of about 0.6 nm between the moment when it is estimated and the next measurement interval of 100 s. This shows that long term temperature variations are a limiting factor to nulling measurements over long periods. A much more stable MMZ would be required to avoid too frequent calibrations and loss of precious observation time.

Results over a 100 s with a calibrated disturbance

The measurements over 100s were repeated with the introduction of the disturbance described in 3.3. Table 2 compares the results obtained with the simple integrator control law and the LQG based one. The disturbance is not well corrected by the integrator. With the LQG control, the measured nulling ratio is only slightly higher than the one measured without the disturbances. This shows the efficiency of the LQG control, if enough flux is available to have the required control bandpass.

Critère	Objectif	Integrateur	LQG
σ_δ [nm rms]	1,7	5,57	1,17
$\langle N_{moy} \rangle_{T=100s}$	10^{-4}	$8,5 \times 10^{-5}$	$1,14 \times 10^{-5}$
$\langle N_{\delta,w} \rangle_{T=100s}$	$3,5 \times 10^{-5}$	$7,3 \times 10^{-5}$	$3,3 \times 10^{-6}$
$\sigma_{N,\tau=1s}$	$1,5 \times 10^{-5}$	3×10^{-6}	3×10^{-7}

Table 2 : nulling ratio over 100 s with 18 nm rms calibrated disturbance, simple integrator or LQG based control law

5. CONCLUSION

Although our test plan is not yet fully completed, we have reached excellent results with PERSEE. The measured 10^{-5} nulling ratio with a 37 % spectral bandwidth and over a 7 h duration is a strong support to the feasibility of space based nulling interferometry. The nulling budget is well mastered and all contributors were experimentally estimated. The major contributor is the opd, which can be controlled to better than 1 nm rms. The tip/tilt internal loop with about 1/100 pixel resolution allows a good control of the flux mismatch through the injection into single mode fibers with tip/tilt active mirrors. The maximum correction is about 200 arcsec to avoid the differential polarization effects to become dominant for a 10^{-5} nulling ratio. With such a fine pointing solution in space, the pointing requirements on the spacecrafts would then be directly imposed by the angular magnification and the required nulling ratio. By instance for PEGASE, with M=40 and 10^{-4} nulling, a 10 arcsec classical pointing is compatible with the mission assuming a 400 arcsec stroke, which is not very demanding. With M=200 and 10^{-5} nulling, one would have to constrain the satellite pointing down to the arcsec level or even lower. Our experimental results also proves the efficiency of the spatial filtering using fluoride glass single mode fibers at the 10^{-5} nulling level.

Furthermore, we prove that we can maintain the nulling result despite quite high disturbance levels. Although this was obtained with very high flux, the implemented LQG based method could be helpful for designing an optimal mission and testing it on ground. The measured data can be used to predict the maximal disturbance frequency that can be corrected for a given mission, assuming a list of targets and a set of basic parameters (the diameter of the collector, the optical transmission,…). The achromatic π-phase shift using field reversal proved to be very efficient and tolerant to about 100 arcsec differential tip/tilt angles (arm a vs arm b) at the 10^{-5} nulling level. As it allows a simple design reducing the use of additional dispersive elements, this technical solution appears the best for a space based mission. The MMZ based architecture of the combiner is also very efficient. The spatial modulation allows a high band pass opd measurement simultaneously with the nulling ratio. This is very important to analyze and correct the opd effects on the performance, both on ground and in flight. The tight integration of the FS and the science channels reduces the differential thermal drifts. Assuming enough funding for a dedicated thermo-mechanical design with a reduced number of adjustable dof, we estimate that this kind of solution can have 60 nm/K thermal sensitivity on the differential opd. Hence a 1 nm differential stability could be reached with a temperature stability requirement of about 10 mK over a 30 cm side box, which seems feasible with standard thermal control techniques, even in non L2 orbits. Last, we developed many calibration and integration procedures, which are very helpful to master such an optical instrument, both on ground and in space.

In the coming year, additional measurements will be made on the bench. First, we will try to acquire and control fringes with initial drifts up to 100 µm/s. Then, the source module will be modified to implement a planet simulator in order to test various image reconstruction methods.

6. REFERENCES

[1] Léger, et al., "The DARWIN project," Astrophysics and Space Science 241, 135-146 (1996).

[2] Léger, A., et al., "DARWIN mission proposal to ESA," ESA's Cosmic Vision Call for Proposals, (2007).

[3] Beichman, C. A., et al., "The Terrestrial Planet Finder (TPF) : a NASA Origins Program to search for habitable planets," (1999).

[4] Lawson, P. R., "Principles of Long Baseline Stellar Interferometry," (2000).

[5] Danchi, W. C., et al., "Scientific rationale for exoplanet characterization from 3-8 microns: the FKSI mission," Proc. SPIE 6268, 626820 (2006).

[6] Ollivier, M., et al., "Pegase, an infrared interferometer to study stellar environments and low mass companions around nearby stars," ESA's Cosmic Vision Call for Proposals, (2007).

[7] J.M. Le Duigou et al., "Pegase: a space-based nulling interferometer," Proceedings of the SPIE 6265, n° 62651M (2006).

[8] Coudé du Foresto, V., et al., "ALADDIN: an optimized nulling ground-based demonstrator for DARWIN," Proc. SPIE 6268, 626810 (2006).

[9] J.M. Le Duigou et al., "Persée: a nulling breadboard coupled with a free flying GNC simulator", Proceedings of the 3rd International Conference on formation Flying, (2008)

[10] Cassaing, F., et al., "Persee: a nulling demonstrator with real-time correction of external disturbances," Proc. SPIE 7013(1), 70131Z (2008).

[11] Houairi, K., et al., "PERSEE, the dynamic nulling demonstrator: Recent progress on the cophasing system," Proc. SPIE 7013, (2008).

[12] Jacquinod, S., et al., "PERSEE: description of a new concept for nulling interferometry recombination and opd measurement," Proc. SPIE 7013, (2008).

[13] Hénault, F. et al., "Review of OCA activities on nulling testbench PERSEE," Proc. SPIE 7734, (2010).

[14] Serabyn, E. et al., "Fully symmetric nulling beam combiners," Appl. Opt. 40(10), 1668-1671 (2001).

[15] J. Lozi et al., "PERSEE: Experimental results on the cophased nulling bench", Proc. SPIE 7734 (2010).

[16] J. Lozi et al., "Current results of the PERSEE testbench: the cophasing control and the polychromatic null rate", Proc. SPIE Volume 8151, 8151-10 (2011).

[17] A. Villien et al., "GNC for the PEGASE mission", 17th IFAC Symposium on Automatic Control in Aerospace (2007).

[18] J.M. Le Duigou, "Microvibration Measurements on Spot 4, Results of the Micromedy Experiment", Proceedings of a European Conference on Spacecraft structures, materials and mechanical testing, ESA-SP, Vol. 428, p475, (1999)

[19] E. Serabyn, "Nulling interferometry : symmetry requirements and experimental results", Proc. SPIE 4006, p328-339, (2001)

[20] J.M. Le Duigou et al, "First results of the PERSEE Experiment", Proceedings of ICSO 2010, Rhodes, Greece, (2010)